Nano Energy (2016) 22, 1–10

Available online at www.sciencedirect.com

ScienceDirect

journal homepage: www.elsevier.com/locate/nanoenergy

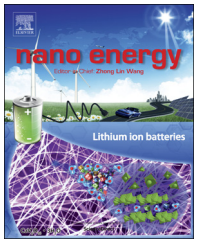

FULL PAPER

Self-doped V^{4+}-V_2O_5 nanoflake for 2 Li-ion intercalation with enhanced rate and cycling performance

Huanqiao Song[a,b,*], **Chaofeng Liu**[a], **Changkun Zhang**[a], **Guozhong Cao**[a,c,*]

[a]*Beijing Institute of Nanoenergy and Nanosystems, Chinese Academy of Sciences, Beijing 100083, China*
[b]*Department of Chemical Engineering, Beijing institute of petrochemical technology, Beijing 102617, China*
[c]*Department of Materials and Engineering, University of Washington, Seattle, WA 98195-2120, United States*

Received 17 September 2015; received in revised form 30 January 2016; accepted 1 February 2016
Available online 8 February 2016

KEYWORDS
Self-doped V^{4+}-V_2O_5 nanoflakes;
Oxygen vacancies;
Structure stability;
Electron/Li-ion transport;
Rate and cycling performance

Abstract
Orthorhombic V_2O_5 has been considered as one of the most promising cathode materials for new lithium ion batteries (LIBs) due to its high specific capacity, easy synthesis and good safety. However, the poor rate and cycling performance of V_2O_5 electrodes significantly impede their applications in high-power and long-life LIBs. The present work reports facile synthesis of self-doped V^{4+}-V_2O_5 nanoflakes through combusting the $NH_4V_4O_{10}$ and VO_2 (B) mixture in the presence of 2-ethylimidazole. The resulting V^{4+}-V_2O_5 exhibited superior rate capability (a reversible capacity of 293, 268, 234, 214, 196 and 139 mA h g^{-1} at 100, 300, 600, 1000, 2000 and 4000 mA g^{-1}, respectively) and remarkable cycling performance (95% capacity retention after 100 discharge/charge cycles at 2000 mA g^{-1}). The outstanding performance is derived from the uniform nanoflake structure, which offers more surface area and reaction sites for lithium ion intercalation, and the presence of tetravalent vanadium ions accompanied with oxygen vacancies, which might promote and catalyze the electrochemical reactions at the surface, in addition to improve the intrinsic electrical conductivity and Li ion diffusion coefficient, as reflected by the smaller polarization and more reversible and easier phase transitions than those of V_2O_5 without detectable V^{4+} and oxygen vacancies.

*Corresponding authors at: Beijing Institute of Nanoenergy and Nanosystems, Chinese Academy of Sciences, Beijing 100083, China.
E-mail addresses: songhuanqiao@bipt.edu.cn (H. Song), gzcao@u.washington.edu (G. Cao).

http://dx.doi.org/10.1016/j.nanoen.2016.02.004
2211-2855/

Introduction

Lithium ion batteries (LIBs) with high energy density and energy conversion efficiency have been widely used in portable electronic devices, electric vehicles and hybrid electric vehicles and made a significant impact in our modern life [1-3]. However, the development of new LIBs with high energy and power densities falls way behind the demands of ever fast advancing electronic devices and electric vehicles. It is imperative to explore new cathode material with larger capacities and higher cycling stability as the energy storage performance of LIBs is limited by cathode [4,5]. Among the potential cathode materials for the next generation LIBs, orthorhombic vanadium pentoxide (V_2O_5) has attracted significant attention lately due to its high specific capacity with 2 lithium-ion reversible intercalation, easy synthesis, high safety, as well as low cost [6-9].

V_2O_5 is composed of distorted VO_6 octahedra linked together to form layered structure and adjacent layers are held together by weak van der Waals forces [10]. Such layered structures make V_2O_5 a good host for the reversible multiple Li-ion insertion and extraction. The reversible theoretical capacity of V_2O_5 is 294 mA h g^{-1} in the voltage range of 4.0-2.0 V *vs.* Li/Li^+, which is almost twice the usually used cathode materials, such as $LiCoO_2$ (140 mA h g^{-1}) and $LiMn_2O_4$ (148 mA h g^{-1}) [11-13]. What makes V_2O_5 cathode material more attractive is their high theoretical capacity and readily achievable and has been demonstrated experimentally [7-14]. However, the practical application of V_2O_5 as cathode of LIBs has been hindered so far largely by its slow Li ion diffusion (10^{-12}-10^{-13} cm^2 s^{-1}), low electrical conductivity (10^{-7}-10^{-6} S cm^{-1}), and poor structure stability, which lead to low rate performance and poor long-term cycling stability [15-17]. To overcome these limitations, extensive research has been carried out [18-21]. Nanostructured V_2O_5 materials with large surface area and short Li ion diffusion distances can mitigate the slow electrochemical kinetics. For example, ultrathin V_2O_5 nanosheets with a large specific surface area of 147.5 m^2 g^{-1} delivered high specific rate capacity of 274 and 137 mA h g^{-1} at 0.2 and 30 C in the voltage range of 2.0-4.0 V [22]. Nanoflakes-assembled three-dimensional hollow-porous V_2O_5 presented a high reversible capacity of 283 mA h g^{-1} at 100 mA g^{-1} with excellent capacity retention even at a current density of 2000 mA g^{-1} (119 mA h g^{-1}) at 2.0-4.0 V [23]. These V_2O_5 nanomaterials indeed exhibited enhanced electrochemical kinetics and buffered volume change, resulting in higher capacity and rate performance than non-nanostructured V_2O_5 [21,23,24]. But it is noteworthy that these nanostructured V_2O_5 still suffered from poor cycling stability because of the low intrinsic electrical conductivity and/or crystal structural fracture during Li insertion/extraction processes. It is known that the surface energy and surface defects have appreciable impacts on electrochemical reactions and lithium ion storage [25,26]. For example, hydrogenated TiO_2 demonstrated fast and stable lithium storage performance due to the presence of Ti^{3+} species that results in high electrical conductivity [27-29]. The presence of V^{4+} in V_2O_5 improved the electrical conductivity and introduced oxygen vacancies, resulting in a much enhanced lithium ion storage performance [25,30]. However, the reported methods to introduce V^{4+}, including heating V_2O_5 under vacuum, inert or reducing conditions (e.g., N_2 or H_2), have the limitations of multiple steps, complicated process and producing a small amount of tetravalent vanadium ions [25,31,32].

This paper reports a simple hydrothermal growth followed with a combustion-treatment for the synthesis of V^{4+} doped V_2O_5 (V-V_2O_5) nanoflakes. To the best of our knowledge, this is the first time that a large number of tetravalent vanadium ions (17.4%) are introduced into V_2O_5 nanoflakes using the method of one-step combustion. When used as cathode material for LIBs, The V-V_2O_5 nanoflakes demonstrated extremely high structural stability and excellent long-term and fast lithium storage capability. V-V_2O_5 nanoflakes have a discharge capacity of 293 mA h g^{-1} at a current density of 100 mA g^{-1} at the 2nd cycle, with a capacity retention of 89% (260 mA h g^{-1}) after 100 cycles, which is nearly 1.3 times that of non-doped V_2O_5 (N-V_2O_5) nanoflakes (200 mA h g^{-1}). Furthermore, the capacities of V-V_2O_5 nanoflakes are about 293, 268, 234, 214, 196 and 139 mA h g^{-1} at the current densities of 100, 300, 600, 1000, 2000 and 4000 mA g^{-1}, respectively, which are superior to those of N-V_2O_5 nanoflakes (about 288, 246, 202, 168, 128 and 77 mA h g^{-1} at the corresponding current densities).

Experimental section

Material preparation

All the starting materials were of analytically pure grade and used directly without any purification. In a typical synthesis, 0.22 g ammonium metavanadate (NH_4VO_3, $\geq$ 99.0%, Sinopharm Chemical Reagent Co., Ltd.) and 0.27 g oxalic acid dihydrate ($C_2H_2O_4 \cdot 2H_2O$, $\geq$ 99.5%, Sinopharm Chemical Reagent Co., Ltd.) were dissolved in 10 ml distilled water under room temperature with constant stirring until dark red solution was obtained. Afterward, 25 ml anhydrous ethanol was added in the above solution and stirred for another 30 min then the homogeneous solution was transferred into 50 ml Teflon lined autoclave and kept at 180 °C for 16 h. After cooling down naturally, 0.5 g 2-ethylimidazole ($C_5H_8N_2$, 98%, Aldrich) was added into the mixture of blue precipitate and solution and magnetically stirred for 15 minutes. Above solution was poured into a crucible and then placed into a preheated oven (400 °C) to undergo combustion. After 2 h reaction time, the final V-V_2O_5 nanoflakes were obtained with no further purification. For comparison, V_2O_5 nanoflakes without introducing V^{4+}, which were denoted as N-V_2O_5 nanoflakes, were also prepared by calcining the blue precipitate (the mixture of $NH_4V_4O_{10}$ and VO_2 (B)) after centrifugation for three times in air at 400 °C for 2 h with a heating ramp of 1 °C min^{-1}.

Material characterization

The crystal phases of the products were investigated by a Bruker powder diffraction system (model D8 Advanced) using a Cu Ka radiation source. Different 2θ angular regions were scanned at a rate of 6° min^{-1} with a step size of 0.02°. Raman spectra were collected at $\pm$0.65 cm^{-1} resolution

with a Horiba JOBIN YVON Raman system (LabRAM HR Evolution) using an argon ion laser (532 nm) as the excitation source. X-Ray photoelectron spectroscopy (XPS) analyses were conducted on a K-Alpha 1063 instrument using monochromated Al-Ka as the X-ray source. Charging effects were corrected by adjusting the binding energy of C from 1 s to 284.6 eV in the XPS spectra. An energy dispersive X-ray spectrometer (EDS OXFORD INCA 300) was used to determine the elemental composition of V_2O_5 nanoflakes. The morphologies of the as-prepared materials were detected by field emission scanning electron microscope (FE-SEM, SU 8020) at 10 kV. TEM investigations were performed using a JEOL JEM-2010 instrument with an accelerating voltage of 200 kV. Thermogravimetric/differential thermal analysis (TGA/DTA) was carried out on a Mettler-Toledo STAR system (TGA/SDTA) from room temperature to 600 °C with a ramping rate of 5 °C min^{-1}. The Brunauer-Emmett-Teller (BET) method was used to calculate the specific surface areas of the as-prepared samples. The electrical conductivities of the prepared samples were measured by the direct current (DC) four-probe technique, as described elsewhere [33,34]. The sample was made into a pellet at a pressure of 100 MPa, and then the pellet was gold coated, dried and sandwiched between stainless steel blocking electrodes for electrical conductivity measurements.

Electrochemical measurements

The working electrode slurry was fabricated by mixing the active material, polyvinylidene fluoride, and Super P conductive carbon in the weight ratio of 70: 10: 20 using N-methylpyrrolidone as solvent. The slurry was then uniformly cast onto Al foil and dried overnight at 80 °C. After solvent evaporation and further dried at 120 °C under vacuum for 12 h, the electrodes were cut into disks and assembled into CR2025 coin type cells in a glove box filled with pure argon. Celgard polypropylene was used as the separator. The electrolyte was 1.0 M $LiPF_6$ in a mixture of ethylene carbonate and dimethyl carbonate (1:1). Li metal was used as the counter electrode and reference electrode. The electrochemical performance of the prepared electrodes was investigated with a Land CT2001A tester system at room temperature. The cells were galvanostatically discharged and charged at different current density within the voltage range of 4.0-2.0 V (*vs.* Li/Li^+). Cyclic voltammetry (CV) tests were carried out using Solartron electrochemical workstation at room temperature at a scan rate of 0.2 mV s^{-1} in the voltage range of 2.0-4.0 V (*vs.* Li/Li^+). The specific capacity and the current density were calculated based on the mass of active material. The mass density of the active material in each electrode disk is 2.0-3.0 mg cm^{-2}. Electrochemical impedance spectroscopy (EIS) was recorded on the Solartron 1287 A in conjunction with a Solartron 1260 A impedance analyzer over the frequency range from 100 kHz to 0.01 Hz and the AC amplitude was 10.0 mV. Before the EIS test, the cells were charged fully and then kept for a period of time to reach a stable state.

Results and discussion

In the hydrothermal process, the blue dark precursor precipitate was synthesized through the reaction between NH_4VO_3 and $C_2H_2O_4$. The color of the precursor is quite similar to that of $NH_4V_4O_{10}$ or VO_2, which indicates the formation of low valence vanadium ions. Generally, $NH_4V_4O_{10}$ or VO_2 can be oxidized to be V_2O_5 when the heating temperature is up to 350 °C in air [35]. In our case, the luteotestaceous V^{4+} doped V_2O_5 was obtained by burning the mixed solution of the precursor suspension and 2-ethylimidazole at 400 °C for 2 h in a muffle oven. The proposed formation reactions of tetravalent vanadium ions were as follows [8,36,37].

$$4NH_4V_4O_{10} + O_2 \xrightarrow{\Delta} 8V_2O_5 + 4NH_3 + 2H_2O \quad (1)$$

$$4VO_2 + O_2 \xrightarrow{\Delta} 2V_2O_5 \quad (2)$$

$$2C_5H_8N_2 + 13O_2 \xrightarrow{\Delta} 8CO + 2CO_2 + 2NO + 2NO_2 + 8H_2O \quad (3)$$

$$V_2O_5 + xCO \xrightarrow{\Delta} V_2O_{5-x} + xCO_2 \quad (4)$$

$$V_2O_5 + xNO \xrightarrow{\Delta} V_2O_{5-x} + xNO_2 \quad (5)$$

During the combustion, $NH_4V_4O_{10}$ and VO_2 are firstly oxidized to be V_2O_5 by O_2 in air at 400 °C, at the same time 2-ethylimidazole decomposes to form CO, CO_2, NO, NO_2, etc. Then some pentavalent vanadium ions in V_2O_5 could be reduced to tetravalent vanadium ions by the reducing gas (CO and NO) and V^{4+} self-doped V_2O_5 materials were achieved [37].

The as-obtained blue dark precipitate was characterized by the XRD technique and the result is presented in Figure 1a. It can be seen that the diffraction peaks of the precipitate can be indexed into the mixed phase of monoclinic $NH_4V_4O_{10}$ (JCPDS No. 31-0075) and monoclinic VO_2 (B) (JCPDS No. 81-2392). And the FESEM images in Figure 1b and c confirm that the precursor precipitate consists of nanoflakes with average length of 800 nm, width of 500 nm and thickness of 40 nm. After combustion or annealing in air at 400 °C for 2 h, the precursor nanoflakes can be safely converted to their corresponding oxides. Figure 2a shows the XRD patterns of the combustion and annealed products. All of the diffraction peaks can be indexed to pure orthorhombic V_2O_5 phase (JCPDS No. 41-1426) for both products, which is consistent with the rapid weight increase before 350 °C because of the oxidation of the mixed precursors into V_2O_5 in the TGA-DTA results (Figure S1). The average grain sizes estimated from (301) peaks using the Debye-Scherrer equation are 36.2 nm and 38.9 nm for V-V_2O_5 and N-V_2O_5, respectively. The morphology and microstructure of V-V_2O_5 are investigated using a FESEM and a TEM. FESEM and TEM images in Figure 2b and c present that the discrete and uniform V-V_2O_5 nanoflake morphology is reserved well during combustion and solid-phase conversion process, except its edge becomes more jagged compared with the precursor nanoflake. While for N-V_2O_5 nanoflakes obtained by annealing the precursor with a heating speed of 1 °C min^{-1}, the morphology of the sample (shown in Figure S2a and b) becomes denser and uneven, though the jagged edges remain. The high-resolution (HR) TEM image of V-V_2O_5 in

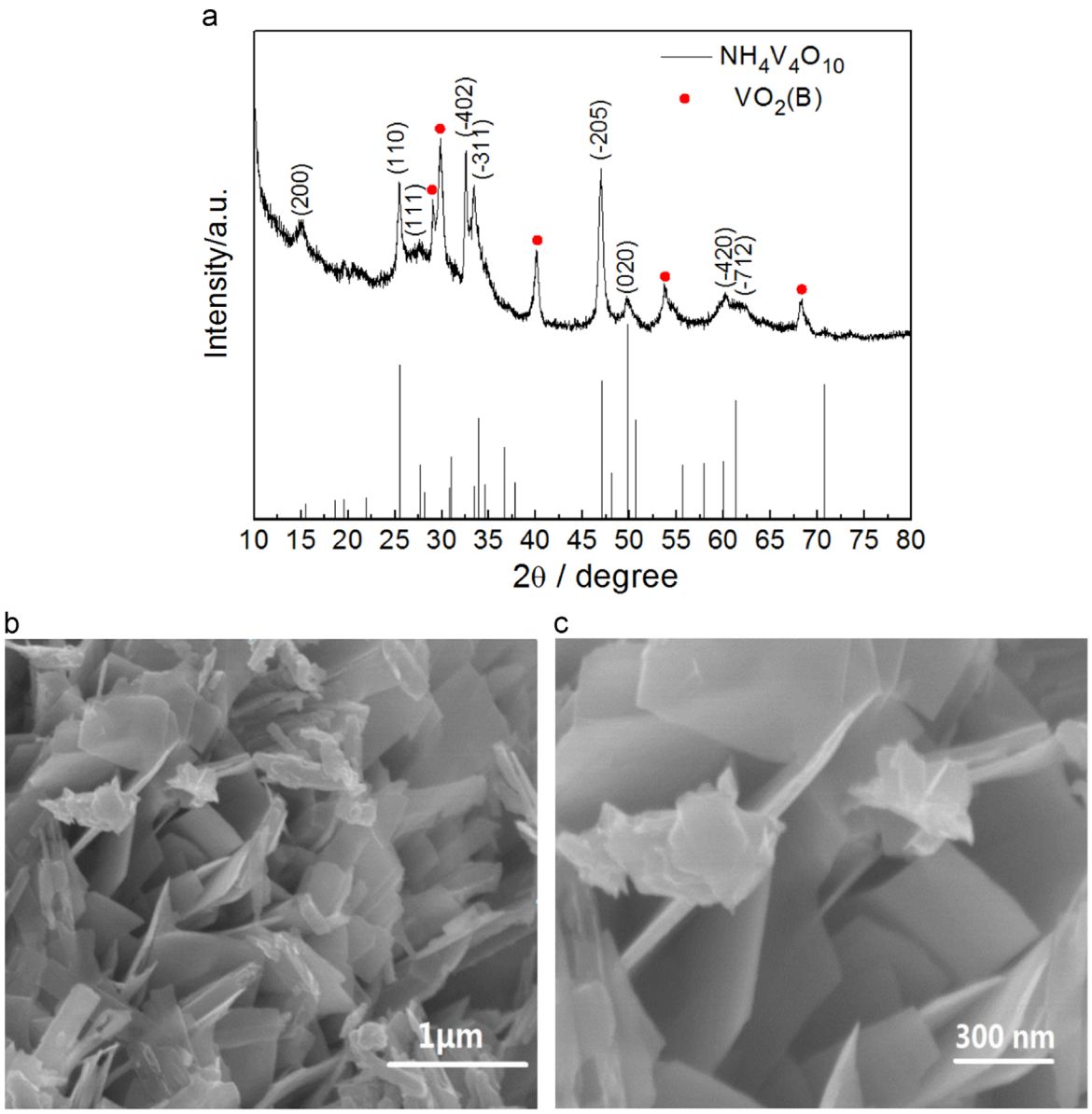

Figure 1 Characterization of the precursor precipitate. (a) XRD patterns. (b and c) Typical FESEM images with different magnifications.

Figure 2d reveals clear lattice fringes with an interfringe spacing of 0.34 nm, which can be ascribed to the (110) planes of V_2O_5. The Brunauer-Emmett-Teller (BET) surface area attained by N_2 sorption analysis are 17.6 $m^2 g^{-1}$ and 16.1 $m^2 g^{-1}$ for V-V_2O_5 and N-V_2O_5, respectively, which agrees well with the observed structure in FESEM images and also corroborates the sizes of nanoflakes. The XPS analysis was used to investigate the differences of surface chemical bonding between V-V_2O_5 and N-V_2O_5 nanoflakes. The V 2p core level spectrum of N-V_2O_5 in Figure 3a shows two peaks at 517.3 eV and 524.9 eV, which correspond to the V $2p_{3/2}$ and V $2p_{1/2}$ peaks for vanadium in the pentavalent state [38]. However, the high resolution XPS of V 2p after fitting presents two peaks of tetravalent vanadium at 516.4 eV (V^{4+} $2p_{3/2}$) and 522.8 eV (V^{4+} $2p_{1/2}$) [39] except for that of pentavalent vanadium for V-V_2O_5 nanoflakes in Figure 3b, suggesting that the partial reduction of the pentavalent ions to tetravalent ions in the V-V_2O_5 sample. The relative molar ratio of V^{5+} to V^{4+} is 4.75:1 calculated based on the peak areas. The presence of V^{4+} in the V-V_2O_5 sample can be ascribed to the reduction atmosphere (CO, NO) during combustion. To maintain the electroneutrality, oxygen vacancies are generated in the lattice of V_2O_5, resulting in $V_2O_{4.826}$. Raman spectra of V-V_2O_5 and N-V_2O_5 in Figure 3c display the typical bands of orthorhombic V_2O_5. However, V-V_2O_5 nanoflake presents a clear broadening of the peaks, which further proves an increased number of oxygen vacancies [40]. The presence of oxygen vacancies could leave more open voids and serve as the possible nucleation centers to facilitate phase transitions [25,41]. In addition, the formation of mixed-valence V^{4+}/V^{5+} is considered to be able to improve the electrical conductivity of the materials [42]. The electrical conductivity of V-V_2O_5 nanoflakes can be obtained based on DC four-probe

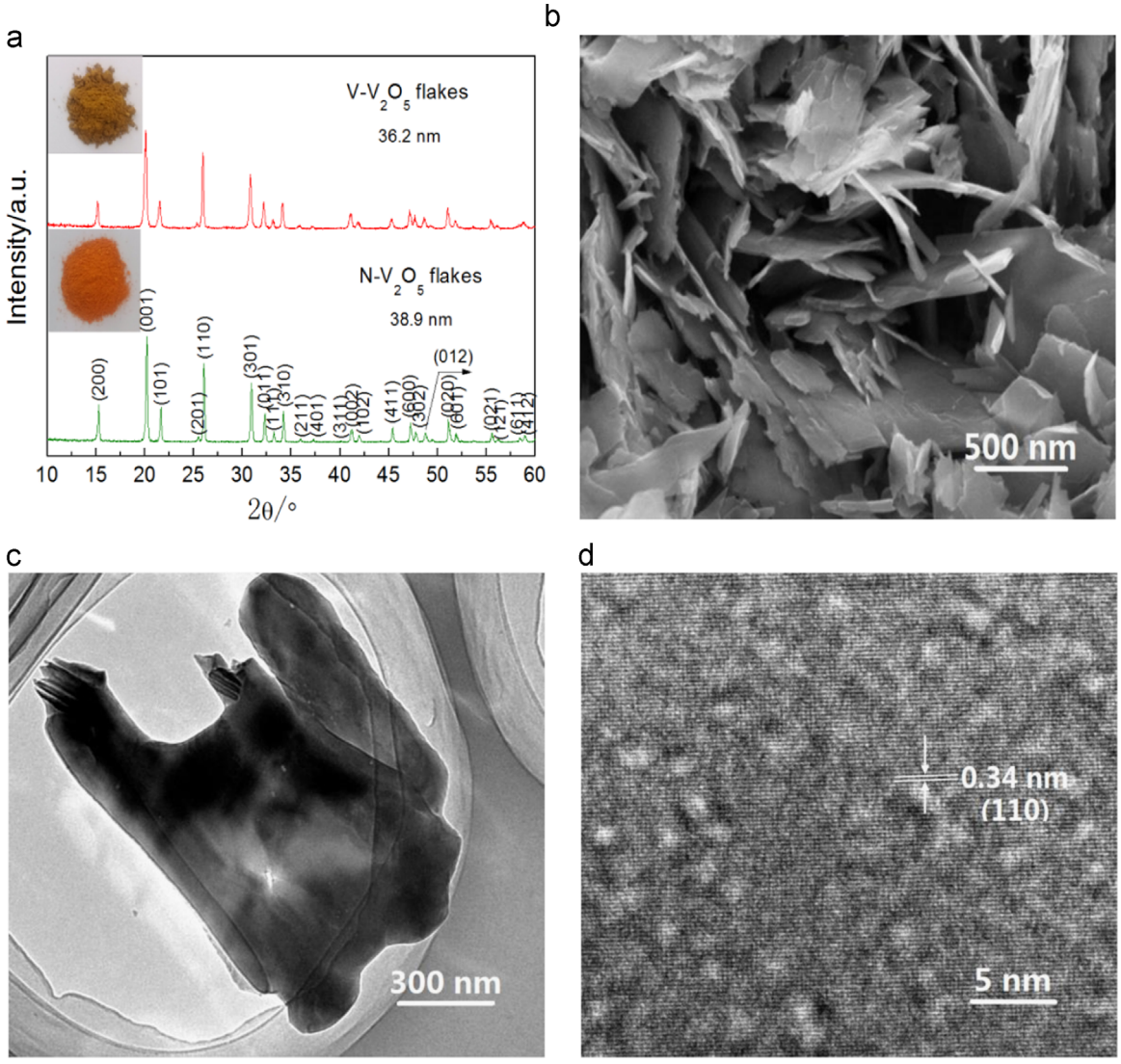

Figure 2 (a) XRD patterns of N- and V-V_2O_5 nanoflakes. (b) FESEM image, (c) TEM image and (d) HRTEM image of V-V_2O_5 nanoflakes.

technique. Currents and voltages attained on the four-probe system for V-V_2O_5 and N-V_2O_5 nanoflakes are shown in Figure 3d. The linear responses of the applied voltage range spectra suggest that the electrical transports are within the ohmic region. The electrical conductivity can be calculated using the current (I) and voltage (V) in Figure 3d by the following expression.

$$\sigma_{dc} = (I/V)(L/A)(S\ cm^{-1}) \quad (6)$$

In Eq. (6), L is the distance between the probes and A is the area of the sample.

The electrical conductivity value of V-V_2O_5 nanoflakes was calculated to be 2.86×10^{-5} S cm^{-1}. This value is at least an order of magnitude higher than the electrical conductivity of N-V_2O_5 nanoflakes where the value is 2.33×10^{-6} S cm^{-1} and the reported data [15,16,24]. Although the exact mechanism is not clear to us at the moment, the presence of 17.4% tetravalent vanadium ions enables the formation of percolated pathways for electron hoping between V^{5+} and V^{4+}, resulting in a significantly increased electrical conductivity.

Figure 4 shows the second-cycle CV profiles of V-V_2O_5 nanoflake and N-V_2O_5 nanoflake electrodes at a scan rate of 0.2 mV s^{-1} in the voltage range of 2.0-4.0 V *vs.* Li^+/Li. Three dominant cathodic peaks at potential of 3.46, 3.18 and 2.34 V are observed for N-V_2O_5 nanoflakes, which correspond to the phase transitions from α-V_2O_5 to ε-$Li_{0.5}V_2O_5$, δ-LiV_2O_5 and γ-$Li_2V_2O_5$, respectively [24,43,44]. In the subsequent anodic process, three obvious oxidation peaks at potentials of 2.53, 3.37 and 3.56 V can be ascribed to the extraction of the two Li ions and the opposite phase transformations to the cathodic reactions. Apart from these peaks, a pair of obvious redox peaks appears in the high potential region (3.57 V/3.68 V), which can be attributed to the phase transition of the γ/γ' system [45]. For the V-V_2O_5 sample, the shape of the CV curve is similar to that of N-V_2O_5. However, some apparent differences are observed though the outlines of the four main redox peaks are observable. The CV plot of V-V_2O_5 sample exhibits more split peaks, for example, the split cathodic peaks at

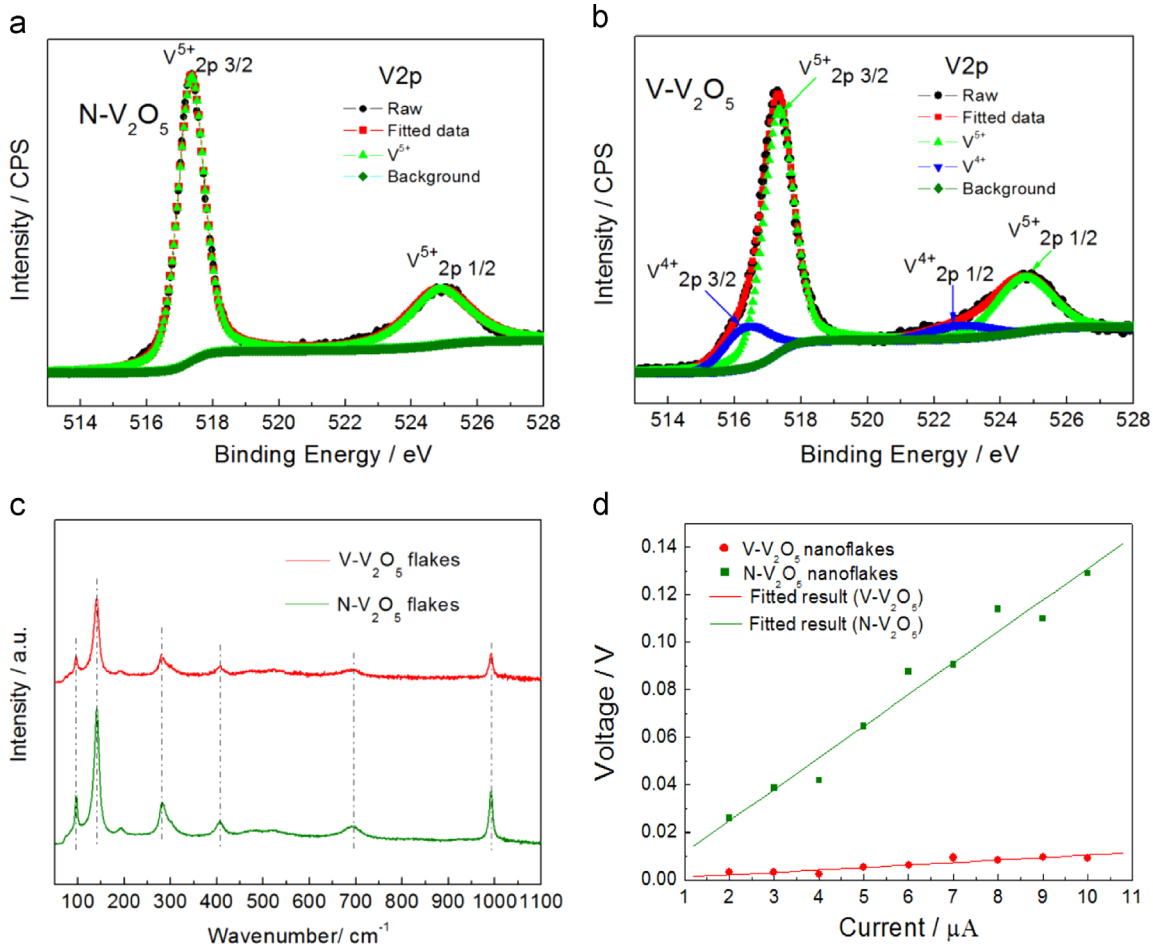

Figure 3 (a and b) XPS spectra for V 2p of N-V_2O_5 and V-V_2O_5, respectively. (c) Raman spectra of N- and V-V_2O_5 nanoflakes. (d) Current-voltage curves obtained by four-probe DC measurement for N- and V-V_2O_5 nanoflakes at room temperature.

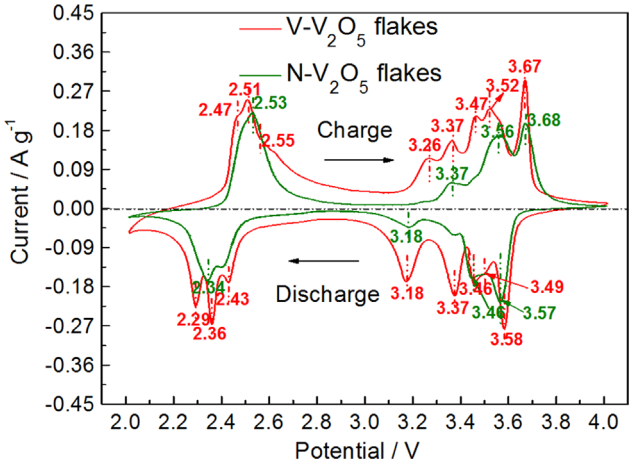

Figure 4 The second-cycle CV profiles of N- and V-V_2O_5 nanoflake electrodes at a scan rate of 0.2 mV s^{-1} in the voltage range of 2.0–4.0 V (*vs.* Li^+/Li).

3.49, 3.46 and 3.37 V and at 2.43, 2.36 and 2.29 V, the split anodic peaks at 2.47, 2.51 and 2.55 V, at 3.26 and 3.37 V and at 3.47 and 3.52 V, which might result from the introduction of tetravalent vanadium ions and the attendant oxygen vacancies. These oxygen vacancies increase surface energy and could possible serve as nucleation centers for easy phase transitions during the lithium ion insertion and extraction processes [38,46]. Therefore, the phase change can take place rapidly. Besides, it can be seen from Table S1 that the peak current densities for V-V_2O_5 nanoflakes are much higher and the potential gaps between the cathodic and anodic peaks are narrower than those of N-V_2O_5 nanoflakes, indicating the faster lithium diffusion speed and the lower polarization between the V-V_2O_5 nanoflakes and electrolyte. A possible explanation for these differences in peak current densities and potential intervals is that intercalation for the N-V_2O_5 electrode is kinetically limited due to its low diffusion coefficient and poor electrical conductivity. However, for V-V_2O_5 nanoflake electrode, the presence of tetravalent vanadium ions and oxygen vacancies makes the redox reactions easier. Furthermore, the more open voids in V-V_2O_5 nanoflake can allow easy accommodation of Li^+ ions during the insertion process, thus lowering the energy barrier for the diffusion process. In the process of anodic scan, similar behaviors are observed. These results indicate that Li-ion diffusion in V-V_2O_5 electrode is more kinetically favorable than that in N-V_2O_5 electrode.

Figure 5a shows the cycling performance of N-V_2O_5 and V-V_2O_5 nanoflake electrodes at 100 mA g^{-1} between 4.0 and 2.0 V. The N-V_2O_5 sample delivers a discharge capacity of 294 mA h g^{-1} at the second cycle, but it quickly decreases to 238 mA h g^{-1} after 33 cycles and 200 mA h g^{-1} after 100

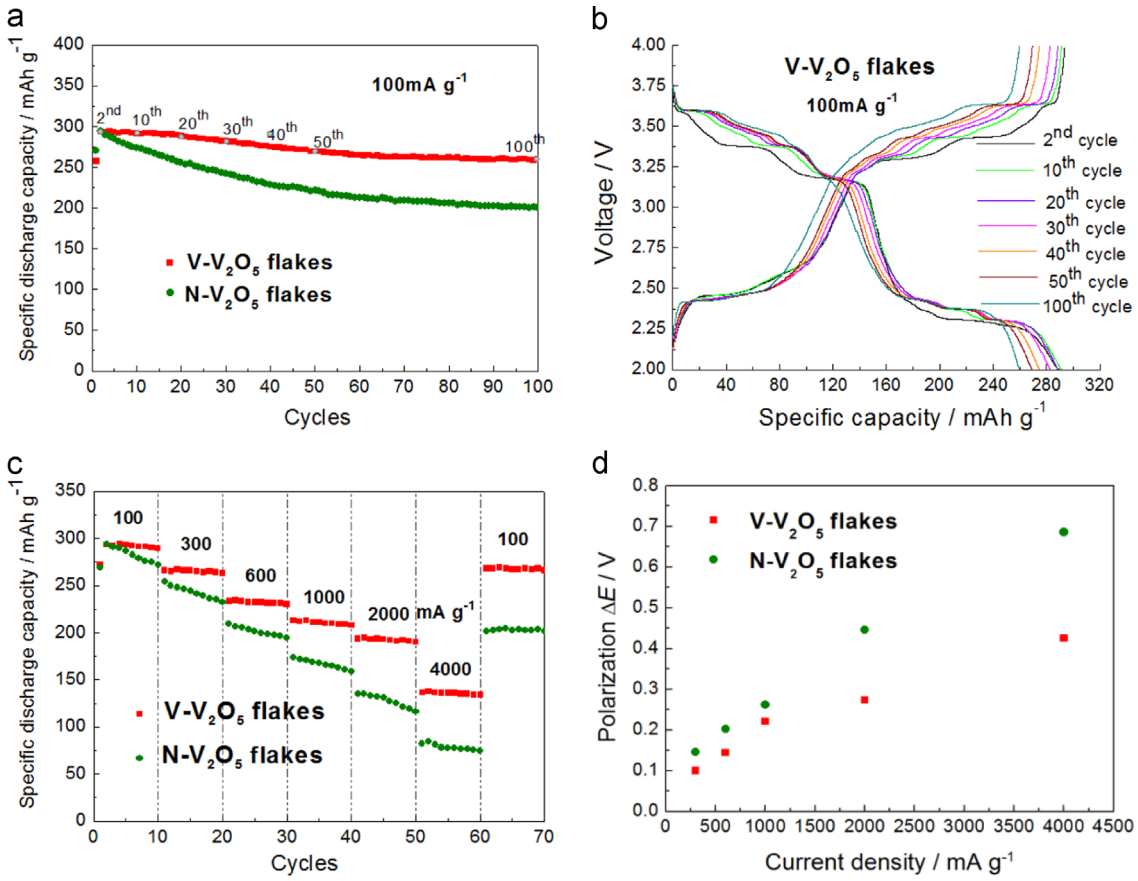

Figure 5 (a) Cycling performance of N- and V-V_2O_5 electrodes at a discharge current density of 100 mA g^{-1}. (b) Discharge-charge voltage profiles of V-V_2O_5 electrode at 100 mA g^{-1}. (c) Rate capability of N- and V-V_2O_5 electrodes at various current rates. (d) Polarization of ΔE *versus* rate plots of N-and V-V_2O_5 electrodes.

cycles. While for V-V_2O_5 nanoflake electrode, the cycling performance is significantly improved. The initial discharge capacity (the second cycle capacity) of V-V_2O_5 electrode is 293 mA h g^{-1} and still remains 260 mA h g^{-1} after 100 cycles. The capacity retention is *ca.* 89% over 100 cycles, indicating the superior cycling stability of V-V_2O_5 nanoflake electrode. It is known that the capacity of V_2O_5 cathode could approach its theoretical limits during early stage of cycling, but capacity fading always appears as a result of continued Li^+ trapping, which come from its intrinsic structural instability, low ionic diffusivity and electrical conductivity. After the introduction of tetravalent vanadium ions and oxygen vacancies, the higher electrical conductivity and easier phase transition lead to the excellent cycling stability during lithium ion insertion and extraction processes. In addition, the discrete and uniform nanostructure also contributes to the high electrochemical stability of V-V_2O_5 nanoflake electrode. Figure 5b gives the representative discharge-charge curves of V-V_2O_5 nanoflake electrode at 100 mA g^{-1}. Eight plateaus are observed at 3.58, 3.49, 3.46, 3.37, 3.18, 2.43, 2.36 and 2.29 V on the discharge curves and eight plateaus are seen at 2.47, 2.51, 2.55, 3.26, 3.37, 3.47, 3.52 and 3.67 V in the charge processes, which are quite agreement with the peaks in CV curve. After cycling, as can be seen, the plateau at 3.58 V in the discharge curves increase evidently, while the plateaus at 3.18 V and 2.29 V exhibit an obvious decrease. In the charge processes, capacity loss within the plateaus from 2.46 to 2.55 V is larger than others. The variations of capacities at different plateaus suggest possible structure self-rearrangement during lithium insertion/extraction processes.

The rate performance was investigated at different current densities, ranging from 100 to 4000 mA g^{-1}. In Figure 5c, it can be seen that the V-V_2O_5 electrode demonstrates higher capacity than the N-V_2O_5 electrode. The discharge capacities of V-V_2O_5 nanoflake electrode are about 293, 268, 234, 214, 196, 139 mA h g^{-1} at the current densities of 100, 300, 600, 1000, 2000, 4000 mA g^{-1}, respectively, while for N-V_2O_5 nanoflake electrode, the discharge capacities maintain 288, 246, 202, 168, 128, 77 mA h g^{-1} at the corresponding current densities. It is noteworthy that the capacities of V-V_2O_5 nanoflakes are close to those of N-V_2O_5 nanoflakes at low current densities, while at high current densities the capacities are obviously higher than those of N-V_2O_5 nanoflakes. To understand the excellent rate capability of V-V_2O_5 nanoflakes, the discharge/charge curves at 300, 600, 1000, 2000, 4000 mA g^{-1} were analyzed for both V- and N-V_2O_5 (Figure S3). The polarization of ΔE was defined as the potential gap between the average charge plateau and the average discharge plateau during the phase transitions from α-V_2O_5 to ε-$Li_{0.5}V_2O_5$ and δ-LiV_2O_5. It can be seen that the ΔE of V-V_2O_5 is 0.100, 0.144, 0.221, 0.273, 0.426 V at 300, 600, 1000, 2000, 4000 mA g^{-1}, which are evidently smaller than

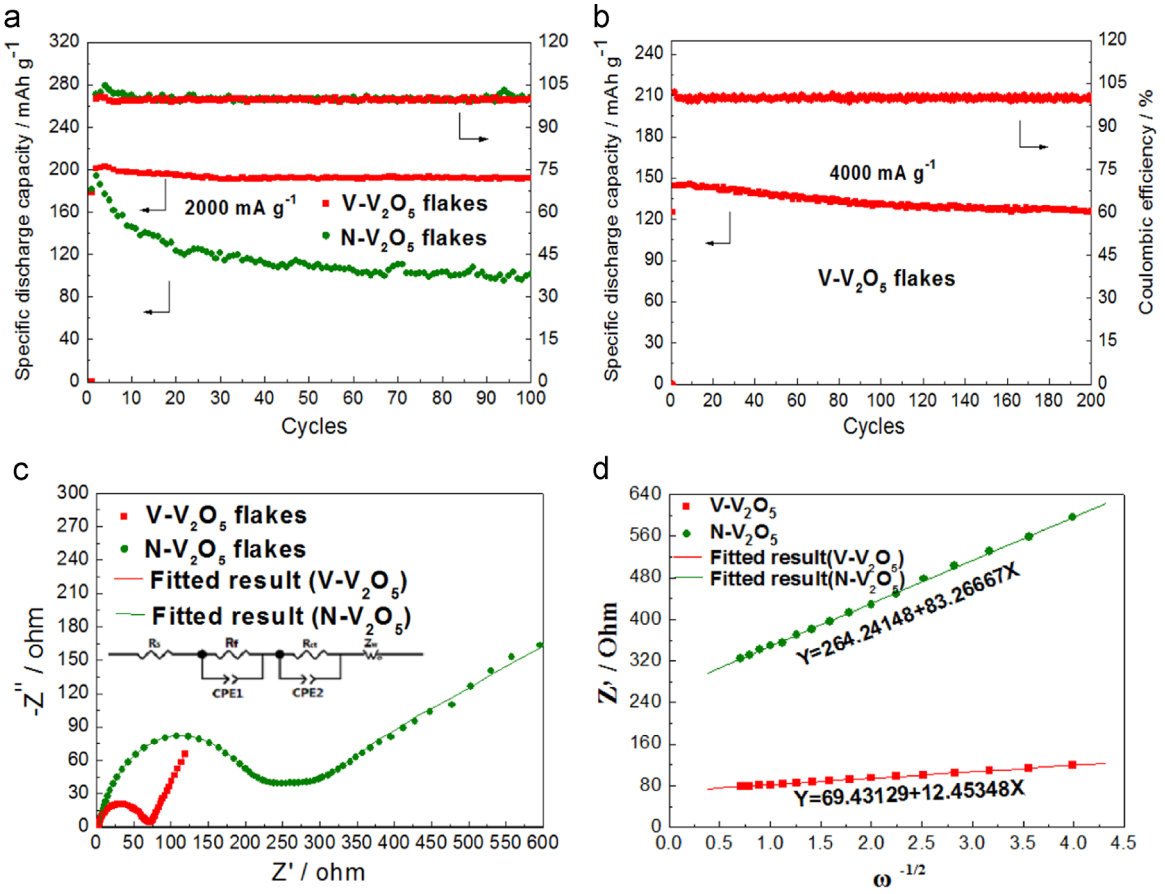

Figure 6 (a) Cycling performance and Coulombic efficiency of N- and V-V_2O_5 nanoflake electrodes at 2000 mA g^{-1}. (b) Cycling performance and Coulombic efficiency of V-V_2O_5 electrode at 4000 mA g^{-1}. (c) Nyquist plots of N- and V-V_2O_5 electrodes at fully charged stage. (d) The relationship curves between Z' and $\omega^{-1/2}$in the low frequency range.

those of N-V_2O_5 nanoflakes (0.146, 0.203, 0.262, 0.446, 0.686 V, respectively) in Figure 5d. The smaller polarization of V-V_2O_5 can be ascribed to its high intrinsic electrical conductivity resulting from the presence of tetravalent vanadium ion, thus resulting in high rate performance in LIBs. After the rate measurement, a capacity of 267 mA h g^{-1} is obtained for the V-V_2O_5 nanoflake electrode when the current density returns to 100 mA g^{-1} at the 61st cycle, while for N-V_2O_5 nanoflake electrode only 202 mA h g^{-1} is observed. In addition, the cycling stabilities of V-V_2O_5 and N-V_2O_5 nanoflake electrodes at high rate of 2000 mA g^{-1} are shown in Figure 6a. The discharge capacity of V-V_2O_5 electrode is 201 mA h g^{-1} at the second cycle and no obvious capacity loss is seen in the following cycles (95% capacity retention at the 100th cycle). However, for N-V_2O_5 electrode, the discharge capacity is as high as 194 mA h g^{-1} at the second cycle, and only remains 101 mA h g^{-1} after 100 cycles. The Coulombic efficiencies for both V-V_2O_5 and N-V_2O_5 electrodes are constant at approximately 100% throughout the overall cycling process. Furthermore, it can be seen in Figure 6b that the capacity of V-V_2O_5 nanoflake electrode can be maintained 87% retention of the initial reversible capacity even after 200 cycles at the current density of 4000 mA g^{-1}. Such high electrochemical stability of V-V_2O_5 nanoflakes can be attributed to their stability of structure, which can be proved by the SEM image after cycling (Figure S4b).

The effects of the tetravalent vanadium ions and the attendant oxygen vacancies on the electrochemical properties were further studied by the comparison of the EIS results of V-V_2O_5 with N-V_2O_5 nanoflake electrodes after three cycles. Figure 6c shows the Nyquist plots of N-V_2O_5 and V-V_2O_5 electrodes. Each Nyquist plot shows a compressed semicircle from the high frequency to medium frequency range, which represents the charge transfer resistance (R_{ct}) and constant-phase element (CPE, describing the double-layer capacitance and considering the roughness of the particle surface), and a slope line at approximately 45° at the low-frequency is attributed to the Warburg impedance (Z_W) which is related to the diffusion of Li ions in the solid matrix. After fitting the second compressed semicircle with the corresponding equivalent electrical circuit model, the R_{ct} value for V-V_2O_5 electrode is 72.8 Ω, which is much lower than that of N-V_2O_5 electrode (263.5 Ω). The evidently reduced R_{ct} at the electrode/electrolyte interface suggests that the V-V_2O_5 naoflake composite possesses faster kinetics for Li^+ ion diffusion and charge transfer. The Li ion diffusion coefficient can be obtained from the low frequency plot using the following Eqs. (7) and (8).

$$Z' = R_e + R_{ct} + \sigma_w \omega^{-1/2} \tag{7}$$

$$D_{Li^+} = \frac{R^2T^2}{2A^2n^4F^4C^2\sigma_W^2} \tag{8}$$

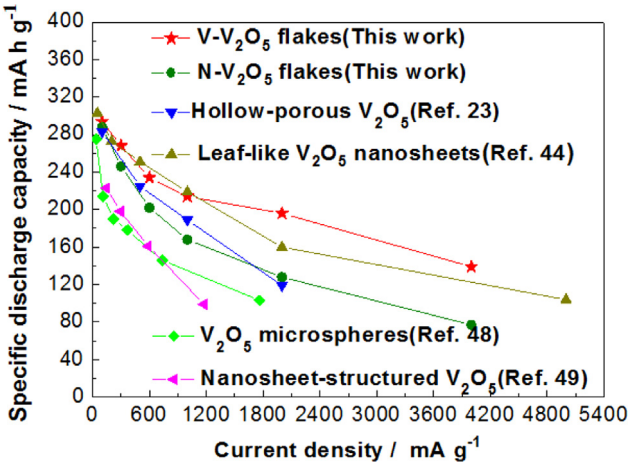

Figure 7 A comparison of electrochemical performance of V-V_2O_5 nanoflakes with N-V_2O_5 nanoflakes and other previous works.

where $\omega(2\pi f)$ is the angular frequency in the low frequency range, R_e andR_{ct} are the kinetics parameters independent of frequency. R is the gas constant, T is the temperature, A is the area of the electrode, n is the number of electron transfer per mole active material involved in the electrode reaction, F is Faraday's constant, and C is the molar concentration of Li ions.

In Eq. (7), there is a linear relationship between Z' and $\omega^{-1/2}$, and the Warburg coefficient (σ_w) can be obtained from the slope of the fitting lines. Using the result of σ_w, the diffusion coefficient (D_{Li^+}) can be calculated according to Eq. (8). Based on the fitting linear equations in Figure 6d, the Li ion diffusion coefficients of N-V_2O_5 and V-V_2O_5 are about 1.71×10^{-12} cm^2 s^{-1} and 1.53×10^{-10} cm^2 s^{-1}, respectively. The Li-ion diffusion coefficient of V-V_2O_5 nanoflakes is 2 orders of magnitude higher than that of N-V_2O_5 sample and the literature data (3.04×10^{-12} cm^2 s^{-1}) [24]. Apparently, the defect sites generated by the reduction atmosphere during combustion facilitate the diffusion of Li-ion in V_2O_5 nanoflakes, thus resulting in excellent electrochemical performance [47].

A comparison of electrochemical performance of V_2O_5 nanomaterials from this study and some representative reported results is shown in Figure 7 [23,44,48,49]. The V-V_2O_5 nanoflakes in this work exhibit both superior rate capability and long cycling performance for the reversible 2 Li-ion insertion and extraction than N-V_2O_5 nanoflakes and the open reported results. Although the exact mechanism for the enhanced electrochemical performance of V-V_2O_5 nanoflakes is complex and needs further study, the high rate capacity and cycling stability can be ascribed to the unique structure advantages of V_2O_5 nanoflakes. First, the discrete and uniform nanoflakes provided high specific surface area and stable structure, which favor the electrolyte penetration and fast Li-ion transport, and accordingly more active material can be utilized effectively and durably at high discharge/charge current density. Second, the presence of mixed-valence V^{4+}/V^{5+} has greatly improved the intrinsic electrical conductivity and reduced the Ohmic polarization of V_2O_5 nanoflakes, thus led to a bigger capacity performance at high rate. Third, in addition to accelerating the phase transition during Li-ion insertion and extraction processes, the oxygen vacancy defects are also favorable for relaxing the strain/stress and maintaining the structural stability during cycling in V_2O_5 nanoflakes [25,50,51]. The introduction of tetravalent vanadium ions and the attendant oxygen vacancies in V_2O_5 nanoflakes can improve the electrochemical reactions greatly at the electrode and electrolyte interface as previous reported in hydrogenated TiO_2 and in doped V_2O_5 [24,52,53].

Conclusions

Self-doped V^{4+}-V_2O_5 nanoflakes with noticeable amount of oxygen vacancies have been successfully prepared by combusting the $NH_4V_4O_{10}$ and VO_2 (B) nanoflake mixture with the presence of 2-ethylimidazole. As cathode materials for LIBs, not only do the resulting V-V_2O_5 nanoflakes exhibit high structural stability but also long-term and fast reversible Li storage capability. The V-V_2O_5 nanoflake electrode can deliver a high reversible capacity of 144 mA h g^{-1} and maintain 87% of the initial capacity after 200 cycles even at an ultra high current density of 4000 mA g^{-1} and it can retain 95% of its starting capacity (201 mA h g^{-1} at the second cycle) at the current density of 2000 mA g^{-1} after 100 cycles. The remarkable electrochemical performance is ascribed to the uniform and stable nanoflake structure and the introduction of tetravalent vanadium ions and the attendant oxygen vacancies, which lead to the structural integrity and improve the intrinsic electrical conductivity and Li ion diffusion coefficient. The results suggest that this self-doped V^{4+}-V_2O_5 nanoflake is a promising alternative cathode material for high-power and long-life LIBs. Moreover, the synthetic approach here reported is relatively simple and general, which may be extended to the design and development of a variety of electrode materials with unique nanostructure containing oxygen vacancies for batteries and supercapacitors.

Acknowledgments

This work was supported by the "thousands talents" program for pioneer researcher and his innovation team, China.

Appendix A. Supplementary material

Supplementary data associated with this article can be found in the online version at http://dx.doi.org/10.1016/j.nanoen.2016.02.004.

Reference

[1] J. Lee, A. Urban, X. Li, D. Su, G. Hautier, G. Ceder, Science 343 (2014) 519–522.
[2] S.Y. Lee, K.H. Choi, W.S. Choi, Y.H. Kwon, H.R. Jung, H.C. Shin, J.Y. Kim, Energy Environ. Sci. 6 (2013) 2414–2423.
[3] J.B. oodenough, Y. Kim, Chem. Mater. 22 (2010) 587–603.
[4] S.T. Myung, K. Amine, Y.K. Sun, J. Mater. Chem. 20 (2010) 7074–7095.
[5] D. Liu, G. Cao, Energy Environ. Sci. 3 (2010) 1218–1237.
[6] M. Chen, X. Xia, J. Yuan, J. Yin, Q. Chen, J. Power Sources 288 (2015) 145–149.
[7] Y.N. Ko, Y. Chan Kang, S.B. Park, Nanoscale 5 (2013) 8899–8903.
[8] H. Song, C. Zhang, Y. Liu, C. Liu, X. Nan, G. Cao, J. Power Sources 294 (2015) 1–7.

[9] C. Zhang, Z. Chen, Z. Guo, X.W. Lou, Energy Environ. Sci. 6 (2013) 974–978.
[10] C. Delmas, H. Cognacauradou, J.M. Cocciantelli, M. Menetrier, J.P. Doumerc, Solid State Ionics 69 (1994) 257–264.
[11] J. Yu, Z. Han, X. Hu, H. Zhan, Y. Zhou, X. Liu, J. Power Sources 262 (2014) 136–139.
[12] M.J. Lee, S. Lee, P. Oh, Y. Kim, J. Cho, Nano Lett. 14 (2014) 993–999.
[13] A.Q. Pan, H.B. Wu, L. Zhang, X.W. Lou, Energy Environ. Sci. 6 (2013) 1476–1479.
[14] Y.Z. Zheng, H. Ding, E. Uchaker, X. Tao, J.F. Chen, Q. Zhang, G. Cao, J. Mater. Chem. A 3 (2015) 1979–1985.
[15] C. Sanchez, R. Morineau, J. Livage, J. Phys. Status Solidi A 76 (1983) 661–666.
[16] M. Benmoussa, E. Ibnouelghazi, A. Bennouna, E.L. Ameziane, Thin Solid Films 265 (1995) 22–28.
[17] C. Wu, F. Feng, Y. Xie, Chem. Soc. Rev. 42 (2013) 5157–5183.
[18] Y. Hu, X. Liu, J. Müller, R. Schlögl, J. Maier, D.S. Su, Angew. Chem. Int. Ed. 48 (2009) 210–214.
[19] Q. Yue, H. Jiang, Y. Hu, G. Jia, C. Li, Chem. Commun. 50 (2014) 13362–13365.
[20] Q. An, P. Zhang, Q. Wei, L. He, F. Xiong, J. Sheng, Q. Wang, L. Mai, J. Mater. Chem. A 2 (2014) 3297–3302.
[21] D. Chao, X. Xia, J. Liu, Z. Fan, C.F. Ng, J. Lin, H. Zhang, Z. X. Shen, H.J. Fan, Adv. Mater. 26 (2014) 5794–5800.
[22] X. Rui, Z. Lu, H. Yu, D. Yang, H.H. Hng, T.M. Lim, Q. Yan, Nanoscale 5 (2013) 556–560.
[23] L. Mai, Q. An, Q. Wei, J. Fei, P. Zhang, X. Xu, Y. Zhao, M. Yan, W. Wen, L. Xu, Small 10 (2014) 3032–3037.
[24] H. Yu, X. Rui, H. Tan, J. Chen, X. Huang, C. Xu, W. Liu, D.Y.W. Yu, H.H. Hng, H.E. Hoster, Q. Yan, Nanoscale 5 (2013) 4937–4943.
[25] D. Liu, Y. Liu, A. Pan, K.P. Nagle, G.T. Seidler, Y.H. Jeong, G. Cao, J. Phys. Chem. C 115 (2011) 4959–4965.
[26] J.S. Chen, Y.L. Tan, C.M. Li, Y.L. Cheah, D. Luan, S. Madhavi, F. Y.C. Boey, L.A. Archer, X.W. Lou, J. Am. Chem. Soc. 132 (2010) 6124–6130.
[27] X. Chen, L. Liu, P.Y. Yu, S.S. Mao, Science 331 (2011) 746–750.
[28] T. Xia, W. Zhang, W. Li, N.A. Oyler, G. Liu, X. Chen, Nano Energy 2 (2013) 826–835.
[29] S.T. Myung, M. Kikuchi, C.S. Yoon, H. Yashiro, S.J. Kim, Y. K. Sun, B. Scrosati, Energy Environ. Sci. 6 (2013) 2609–2614.
[30] D. Liu, Y. Liu, B.B. Garcia, Q. Zhang, A. Pan, Y.H. Jeong, G. Cao, J. Mater. Chem. 19 (2009) 8789–8795.
[31] T.D. Kang, J.S. Chung, J.G. Yoon, Phys. Rev. B 89 (094201) (2014) 1–6.
[32] S.F. Olive-Mendez, C.R. Santillan-Rodriguez, R.A. Gonzalez-Valenzuela, F. Espinosa-Magana, J.A. Matutes-Aquino, Nanoscale Res. Lett. 9 (2014) 1–7.
[33] P. Samarasingha, D.H. Tran-Nguyen, M. Behm, A. Wijayasinghe, Electrochim. Acta 53 (2008) 7995–8000.
[34] A. Wijayasinghe, B. Bergman, C. Lagergren, Solid State Ionics 177 (2006) 165–173.
[35] S. Liang, Y. Hu, Z. Nie, H. Huang, T. Chen, A. Pan, G. Cao, Nano Energy 13 (2015) 58–66.
[36] Y. Wang, Z. Zhang, Physica E 43 (2011) 1726–1729.
[37] F. Zuo, L. Wang, T. Wu, Z. Zhang, D. Borchardt, P. Feng, J. Am. Chem. Soc. 132 (2010) 11856–11857.
[38] G.A. Sawatzky, D. Post, Phys. Rev. B 20 (1979) 1546–1555.
[39] Y. Feng, Y. Li, F. Hou, J. Power Sources 187 (2009) 224–228.
[40] X.Y. Pan, X.M. Ma, J. Solid State Chem. 177 (2004) 4098–4103.
[41] H. Song, Y. Liu, C. Zhang, C. Liu, G. Cao, J. Mater. Chem. A 3 (2015) 3547–3558.
[42] P. Gomez-Romero, Adv. Mater. 13 (2001) 163–174.
[43] C. Niu, J. Li, H. Jin, H. Shi, Y. Zhu, W. Wang, M. Cao, Electrochim. Acta 182 (2015) 621–628.
[44] Y. Li, J. Yao, E. Uchaker, J. Yang, Y. Huang, M. Zhang, G. Cao, Adv. Energy Mater 3 (2013) 1171–1175.
[45] R. Baddour-Hadjean, A. Marzouk, J.P. Pereira-Ramos, J. Raman Spectrosc. 43 (2012) 153–160.
[46] P. Qin, G. Fang, W. Ke, F. Cheng, Q. Zheng, J. Wan, H. Lei, X. Zhao, J. Mater. Chem. A 2 (2014) 2742–2756.
[47] F.C. Frank, Discuss. Faraday Soc. 23 (1957) 122–127.
[48] S. Wang, Z. Lu, D. Wang, C. Li, C. Chen, Y. Yin, J. Mater. Chem. 21 (2011) 6365–6369.
[49] S. Liang, M. Qin, Y. Tang, Q. Zhang, X. Li, X. Tan, A. Pan, Met. Mater. Int. 20 (2014) 983–988.
[50] W.Y. Ma, B. Zhou, J.F. Wang, X.D. Zhang, Z.Y. Jiang, J. Phys. D: Appl. Phys. 46 (105306) (2013) 1–8.
[51] K.E. Swider-Lyons, C.T. Love, D.R. Rolison, Solid State Ionics 152 (2002) 99–104.
[52] Z. Zhang, Z. Zhou, S. Nie, H. Wang, H. Peng, G. Li, K. Chen, J. Power Sources 267 (2014) 388–393.
[53] Y. Li, J. Yao, E. Uchaker, M. Zhang, J. Tian, X. Liu, G. Cao, J. Phys. Chem. C 117 (2013) 23507–23514.

Dr. Huanqiao Song is now working at department of chemical engineering, Beijing Institute of Petrochemical Technology. In 2013, she worked in Prof. Guozhong Cao's group at Beijing Institute of Nanoenergy and Nanosystems as an assistant research scientist (2013-2015). Her current research is focused on the design and development of nanostructured electrode materials for lithium-ion batteries, supercapacitors and fuel cells.

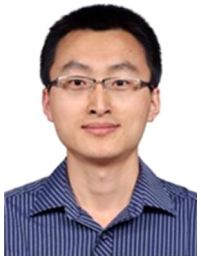

Chaofeng Liu received his BSc and MSc degrees from Central South University. He is currently a PhD candidate under the supervision of Prof. Guozhong Cao at Beijing Institute of Nanoenergy and Nanosystems, Chinese Academy of Sciences. His research interests focus on electrode materials for electrochemical energy storage, such as alkali-ion batteries and hybrid capacitors.

Dr. Changkun Zhang is a postdoc in Beijing Institute of Nanoenergy and Nanosystems, Chinese Academy of Sciences; National Center for Nanoscience and Technology (NCNST). He received PhD degree from the Dalian Institute of Chemical Physics, Chinese Academy of Sciences in 2014. His main research interest is the design and study on the nano-structured materials for batteries and fuel cells.

Guozhong Cao is Boeing-Steiner professor of Materials Science and Engineering, professor of Chemical Engineering and adjunct professor of Mechanical Engineering at the University of Washington, Seattle, WA, and also a senior professor at Beijing Institute of Nanoenergy and Nanosystems and a professor at Dalian University of Technology, China. His current research focused on chemical processing of nanomaterials for solar cells, batteries, and supercapacitors as well as actuators and sensors.